Chemical Science

ROYAL SOCIETY OF CHEMISTRY

EDGE ARTICLE

View Article Online
View Journal

Cite this: DOI: 10.1039/d6sc01505k

All publication charges for this article have been paid for by the Royal Society of Chemistry

Tunable synaptic memory response using organic regioisomeric donor–acceptor–donor luminophore triads

Mainak Bose,†[a] Manoj Kangsabanik,†[b] Dibyendu Dey,†[a] Panče Naumov,*[cdef] Rabindra Nath Gayen*[b] and Manas K. Panda*[a]

Modeling synaptic memory with small molecular compounds allows for replication of key features of biological learning and memory in a simplified, controllable, and tunable chemical system, where processes such as signal transmission, plasticity, and information storage can be realized without the complexity of the full biological networks. Aimed at probing the substitution effects on the molecular conjugation and optoelectronic and neuromorphic performance, here we report novel regioisomeric donor–acceptor–donor (DAD) fluorophores that are utilized for optoelectronic synaptic memory devices. The photophysical characterization revealed substitution-dependent solid-state luminescence across the visible spectrum and variation in lifetimes that are attributed to the combination of molecular packing and charge-transfer characteristics. Diffraction methods and theoretical calculations elucidated the structure–property relationships, highlighting the effect of regiochemistry on the π–π interactions and molecular orbitals. The materials display synaptic memory responses in two-terminal organic devices, demonstrating key neuromorphic functionalities such as paired-pulse facilitation and long-term potentiation. This study introduces design guidelines for multifunctional organic semiconductors by regioisomerism, with potential applications extending to solid-state lighting, sensing, memory devices, and bioinspired computing.

Received 22nd February 2026
Accepted 13th May 2026

DOI: 10.1039/d6sc01505k

rsc.li/chemical-science

Introduction

In the age of artificial intelligence, rapid advancements are being pursued in the fields of data perception for human–machine interfaces, robotics, and prosthetic technologies. The human visual system is an impressive biological tool capable of both perception and processing of photo stimuli (input data) *via* a variety of synaptic plasticity rules—including both volatile and non-volatile components—to channelize various information to the brain. Within the human visual system, the synaptic plasticity describes the brain's capacity to acclimate and reorganize its neural connections, especially at the synaptic level, in response to sensory information. This adaptability enables perceptual learning, visual change, and adaptation to variations in the intensity and colour of light. Replicating such functionalities of the natural visual system by artificial synaptic devices is known to pose significant challenges with photoresponsive efficiency, integration of distinct components, compatibility, energy consumption, and processability.[1–3] Various inorganic materials, including metal oxides, 2D materials, and perovskites, have been employed in artificial optoelectronic devices to emulate the synaptic memory behaviour, with notable success documented recently.[4–15] Conversely, organic crystalline materials have only recently garnered attention as flexible optoelectronic and memory components, primarily due to the ease of their synthesis, relatively lower toxicity, affordability, solution-based processibility under ambient conditions, and the unrivalled opportunities they provide for tuning their properties through molecular design.[16–31] The intrinsic advantages brought about by electron delocalization and defect-induced charge trapping favour donor–acceptor charge-transfer conjugated molecules with planar or rigid structures as materials for organic field-effect transistors and memory devices.[32] These organic materials act as photoabsorbers in three-terminal devices where photoexcitation, under an external electric potential from the gate electrode, mimics the presynaptic event, and the subsequent response current between the source and drain electrodes is analogous to

[a]Department of Chemistry, Jadavpur University, Kolkata-700032, India. E-mail: manaspanda.chemistry@jadavpuruniversity.in
[b]Department of Physics, Jadavpur University, Kolkata-700032, India. E-mail: rgayen.physics@jadavpuruniversity.in
[c]Smart Materials Lab, Division of Science and Mathematics and Smart Materials Lab, New York University Abu Dhabi, 129188 Abu Dhabi, United Arab Emirates
[d]Center for Smart Engineering Materials, New York University Abu Dhabi, 129188 Abu Dhabi, United Arab Emirates
[e]Research Center for Environment and Materials, Macedonian Academy of Sciences and Arts, MK-1000 Skopje, Macedonia
[f]Molecular Design Institute, Department of Chemistry, New York University, New York, New York 10003, USA. E-mail: pance.naumov@nyu.edu
† These authors contributed equally to this work.

the post synaptic event. Such artificial organic architectures essentially replicate the cognitive operation of biological synaptic organs, exemplified by paired pulse facilitation (PPF), long- and short-term plasticity (LTP and STP), excitatory postsynaptic current (EPSC), spike-number-dependent plasticity (SNDP), and conversion from volatile to non-volatile memory states.[10,12,14] Various mechanisms of photosynaptic functions, including charge carrier trapping,[9,19] photoactive electrets, and oxygen-induced defects,[1,2,7,18] have been proposed. Despite notable progress, the development of multifunctional organic molecules that can withstand the challenges of facile synthesis, structural and property tunability, alongside superior capabilities as synaptic memory devices, remains elusive.

Herein, we report a series of donor–acceptor–donor (DAD) type regioisomeric luminescent organic triads that function conceptually equivalent to light-responsive synaptic memory elements, with the device behaviour being determined by isomerism (Fig. 1a and b). These DAD molecules exhibit a criss-cross type 3D molecular arrangement featuring void channels that facilitate charge carrier transport and trapping necessary for synaptic memory function. The molecules, prepared in a single step, contain a cyanostilbene acceptor (A) core with two terminals containing -OMe donor (D) groups in various dispositions (Fig. 1b). The regioisomeric variation in the donor on the phenyl ring was found to strongly impact both the fluorescence properties and the photosynaptic memory response with

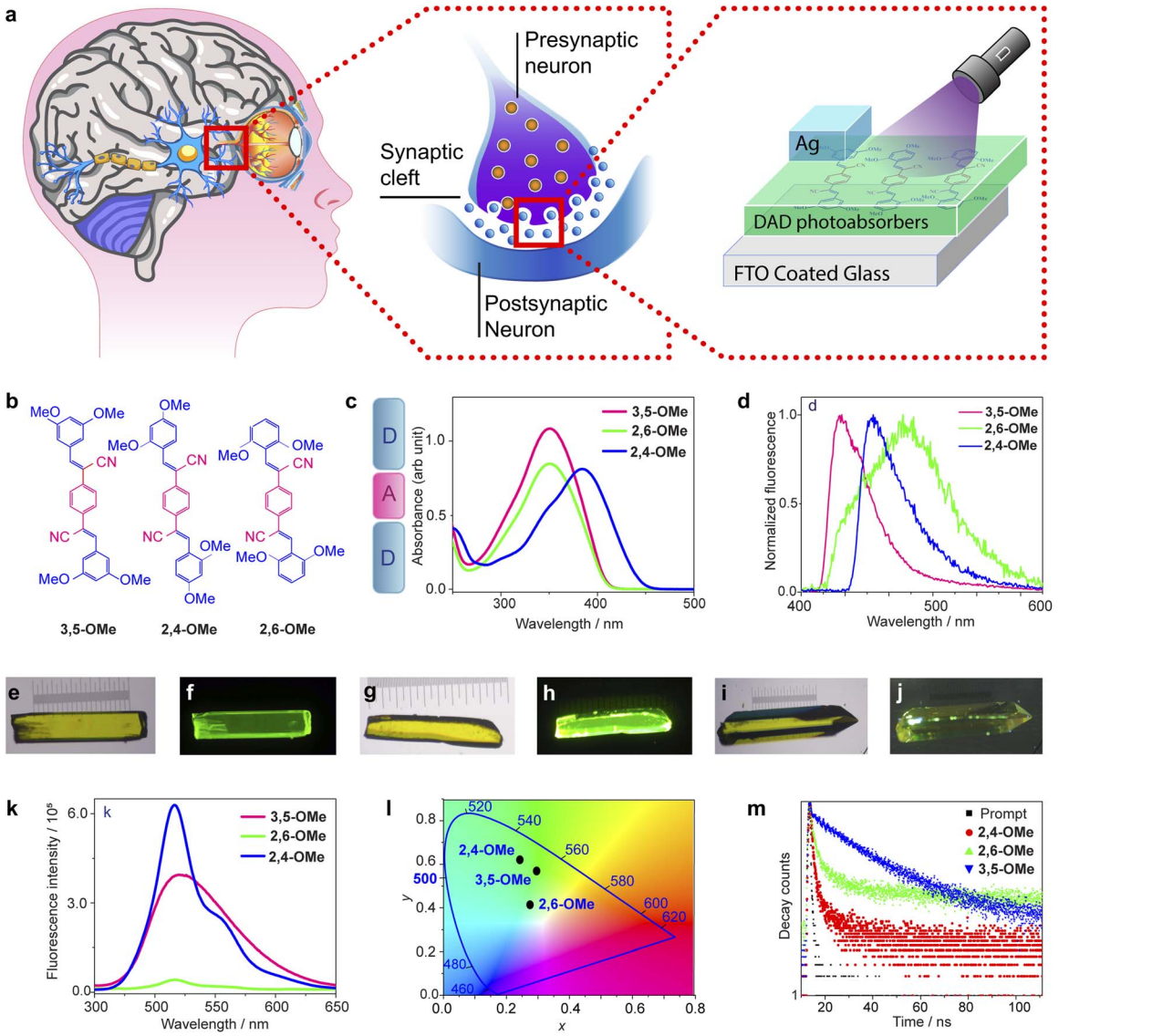

Fig. 1 (a) Model representation of the function of the synaptic memory organ and artificial device. (b) Chemical structures of the donor–acceptor–donor (DAD) type isomers. The DAD components in the structures and the sketch are highlighted in different colors. (c and d) Absorbance (c) and normalized fluorescence (d) spectra recorded in a chloroform solution. (e–j) Microscopic images of the crystals with a 1 mm scale bar in red colour: (e) **3,5-OMe** crystal under ambient light and (f) under UV light, (g) **2,4-OMe** crystal under ambient light and (h) under UV light, and (i) **2,6-OMe** crystal under ambient light and (j) under UV light. (k) Solid-state fluorescence spectra of the DAD isomers. (l) Emission of the isomers on a CIE-1931 plot with *x*, *y* coordinates: **3,5-OMe** (0.294, 0.569); **2,4-OMe** (0.244, 0.619); **2,6-OMe** (0.274, 0.415). (m) Fluorescence decay curves of the three isomers.

various pulses and very high photoconductivity. This approach introduces a new dimension to materials design of neuromorphic electronics, where the synergistic application of light and molecular design is used to control artificial synaptic functions. To our knowledge, this report is the first demonstration in which regioisomerism alone can tune synaptic memory responses in optoelectronic devices, thereby combining molecular chemistry with advanced neuromorphic functionality.

Results and discussion

The compounds were synthesized by a one-step Knoevenagel condensation between *p*-xylylene dicyanide and the respective aldehydes in moderate to good yields (SI Scheme S1) and characterized using standard methods (Fig. S1–S10, SI). As Fig. 1b depicts, the isomers differ from each other by the -OMe substitution on the terminal phenyl rings, while they share the common central acceptor moiety, and all are extensively conjugated. The UV-Vis spectra (chloroform, 1×10^{-5} M) of **3,5-OMe** and **2,6-OMe** contain peaks from the π–π* transition with maximum absorption $\lambda_{max} = 351$ nm and 349 nm for the two compounds, respectively. The absorption of **2,4-OMe** is red-shifted relative to the other two isomers, to 384 nm, due to the combined electronic contribution of the *ortho*- and *para*-substitution that effectively decreases the HOMO–LUMO gap. In contrast, the steric crowding at the two *ortho*-positions in the **2,6-OMe** isomer leads to a non-planar, twisted structure and gives rise to high-energy absorption maxima.

All the isomeric compounds are poorly emissive in solution (Fig. 1d). However, unlike **2,6-OMe**, the two other compounds are strongly emissive in the solid state. As observed from Fig. 1k, the spectrum of the crystal of **2,4-OMe** contains two emission bands with $\lambda_{max} = 516$ nm and a shoulder at 556 nm (CIE coordinates: 0.244, 0.619; Fig. 1l). **3,5-OMe** exhibits broad, structureless emission around 521 nm (CIE coordinates: 0.294, 0.569). The decay of the fluorescence of **2,4-OMe** is bi-exponential, with lifetimes of 2.445 ns (50.88%) and 16.498 ns (49.12%), while that of **3,5-OMe** was fitted with a single-exponential function that afforded a lifetime of 17.445 ns (Fig. 1m and SI Table S1). In contrast to these isomers, **2,6-OMe** is poorly emissive in both the solid state and in solution (Fig. 1i–k), and shows a weak emission at $\lambda_{max} = 516$ nm (CIE coordinates: 0.274, 0.415). This is likely due to the presence of two *ortho*-dispositioned bulky -OMe groups, which cause the molecule to be twisted and disrupt the conjugation between the donor and the acceptor.

Density functional theory (DFT) calculations support the above conclusions, indicating the smallest HOMO–LUMO gap for **2,4-OMe** (3.21 eV) and the highest for **2,6-OMe** (3.50 eV), with **3,5-OMe** having an intermediate value (3.41 eV). The experimental band gaps were calculated from the respective solid state absorption spectra using Tauc plots, corroborating the above trend (Fig. S11, SI). The LUMOs are spread mostly across the central core of all molecules, while the HOMOs reside mostly on the terminal phenyl rings containing -OMe groups (Fig. 2). These variations in emission reflect their "tunability" by means of altering the position of the donor functional groups. Excited-state calculations, performed by using the TDDFT method to examine the transitions responsible for the emission, identified the π–π* transition at 438.8 nm from the HOMO−1 to LUMO+1 level, with an excitation energy of 2.83 eV and an oscillator strength of 1.94, as the major contributor to the emission in **2,4-OMe**. In the case of **3,5-OMe**, the 344.9 nm band was calculated as π–π* transition at 3.60 eV with an oscillator strength of 1.74 and occurs between the HOMO and LUMO levels. In contrast with the other two isomers, however, **2,6-OMe** exhibits a gap of 4.09 eV and an oscillator strength of 0.11 due to a π–π* transition from the HOMO−2 to LUMO energy level corresponding to a wavelength of 303.2 nm. The lower strength of the oscillator corresponding to the transition in the **2,6-OMe** isomer is in accord with its weak emission and can be traced back to its twisted molecular conformation (see below).

The observed significant substituent effects on the solid-state luminescence and other optoelectronic properties were rationalized by the crystal structures of all isomers (Fig. 3 and SI Table S2). The experimental powder X-ray diffraction patterns of the samples matched well their simulated (from the crystal structure) counterparts and confirmed the phase purity of all compounds (Fig. S12–S14, SI). As shown in Fig. 3, while the molecular conformations of **3,5-OMe** and **2,4-OMe** are nearly planar, that of **2,6-OMe** is twisted. In **3,5-OMe** and **2,4-OMe**, the terminal phenyl rings are nearly coplanar with the central phenyl ring (interplanar angles: ∼4.7° and ∼2.9°, respectively, Fig. 3a, b and S15, SI), suggesting strong electronic communication within the DAD skeleton. Both **3,5-OMe** and **2,4-OMe** adopt a slip-stacked J-type aggregation with slip angles ∼48° and 27°, respectively (Fig. 3d, e and S16, SI). The small slip-angles in **3,5-OMe** and **2,4-OMe** facilitate stacking between the layers, enhance the donor–acceptor charge-transfer interaction, and result in red-shift in the emission (Fig. 1k). In contrast to the other two isomers, as is clearly observed from the over-lapped molecular representation in Fig. 3g, the molecule of **2,6-**

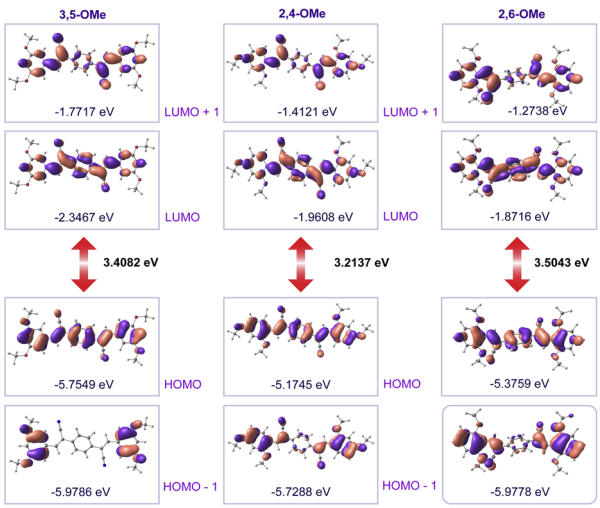

Fig. 2 DFT (B3LYP/6-31G*)-calculated electron isosurfaces of the frontier molecular orbitals of the isomeric compounds.

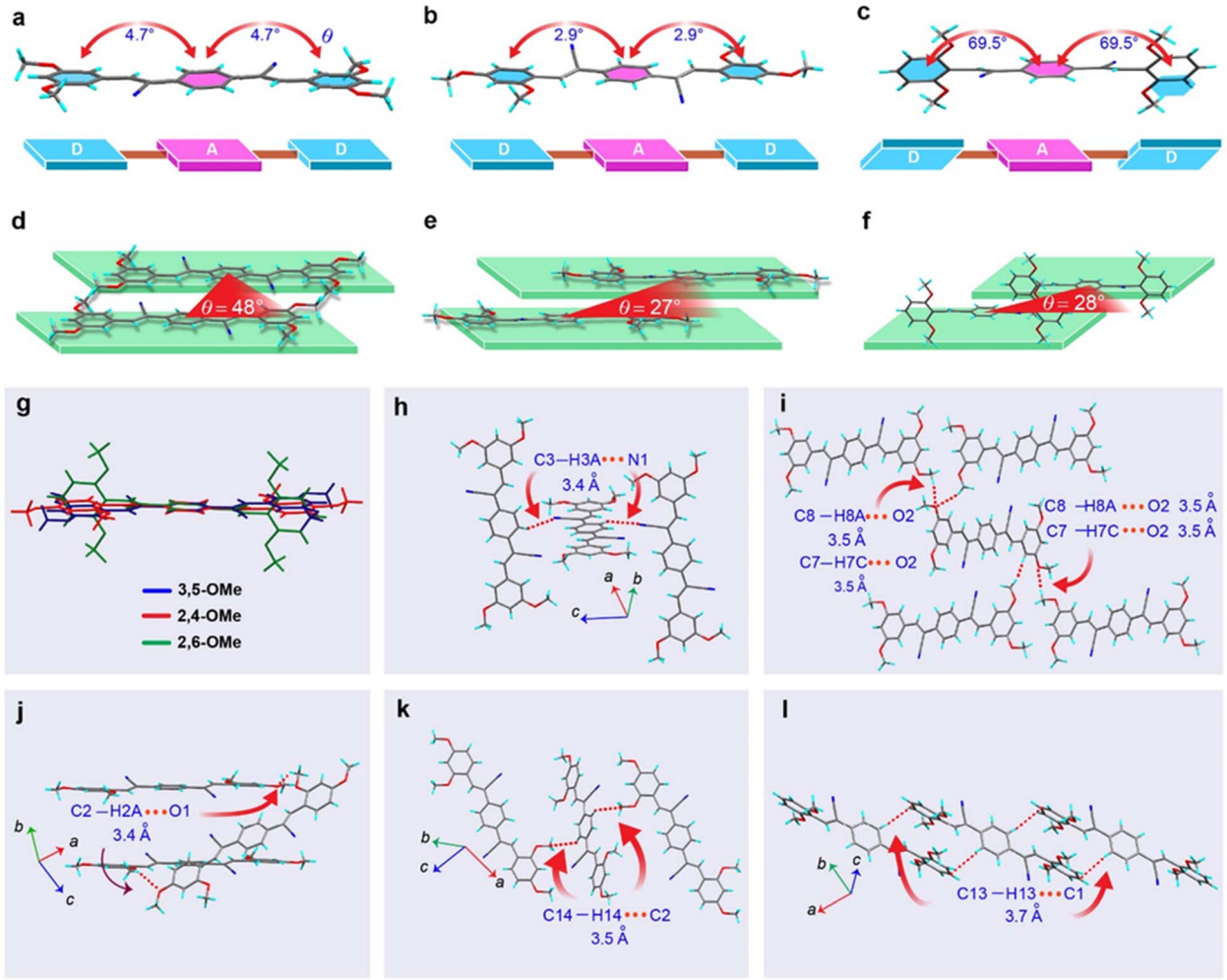

Fig. 3 (a–c) Molecular conformations in the crystals of **3,5-OMe** (a), **2,4-OMe** (b), and **2,6-OMe** (c). (d–f) Slip-stacked disposition and associated angles in the structures of **3,5-OMe**, **2,4-OMe**, and **2,6-OMe**. (g) Overlaid representation of the experimentally determined conformations of the three isomers. (h–l) Intermolecular interactions in the crystal lattices of **3,5-OMe** (h and i), **2,4-OMe** (j and k), and **2,6-OMe** (l).

OMe is twisted due to steric crowding of the -OMe groups, with an angle of ~69.5° between its terminal and central benzene rings (Fig. 3c). This molecular distortion, as pointed out above, accounts for the quenching of fluorescence in the solid state.

Crystallographic face indexing, simulated crystal habits, and analysis of the molecular packing are provided in Fig. S17–S20, SI. In the structure of **3,5-OMe**, hydrogen bonds between the nitrile group and aromatic protons of the central ring (C3–H3A···N1, d(C3···N1) = 3.4 Å, ∠(C3–H3A···N1) = 143.4°) connect the neighbouring molecules and extend roughly along the crystallographic c-axis (Fig. 3h and i). O···H interactions involving methoxy oxygen and methyl protons (C8–H8A···O2, d(C8···O2) = 3.5 Å, ∠(C8–H8A···O2) = 163°; C7–H7C···O2, d(C7···O2) = 3.5 Å, ∠(C7–H7C···O2) = 157.2°) are also present in the crystal lattice. The planar and rigid conformation allows for J-type aggregation with opportunity for intramolecular exciton coupling and results in strong fluorescence (Fig. S16, SI). The molecules in the crystal of **2,4-OMe** adopt a more planar (interplanar angle, 3.0°) and rigid geometry, supported by hydrogen bonding involving the methoxy oxygen atom and neighbouring methoxy hydrogen atoms (C2–H2A···O1, d(C2···O1) = 3.4 Å, ∠(C2–H2A···O1) = 136.8°, Fig. 3j and k) and a weak, non-classical interaction (C14–H14···C2, d(C14···C2) = 3.5 Å, ∠(C14–H14···C2) = 124.3°, Fig. 3j and k). In the case of **2,6-OMe**, the sterically twisted molecules in the lattice are arranged in an antiperiplanar fashion. Except for a weak hydrogen bond (C13–H1···C1, d(C13···C1) = 3.7 Å, ∠(C13–H13···C1) = 149.7°, Fig. 3l), no other intermolecular interactions were observed.

Considering that pores and voids in the crystal lattice usually play important roles in charge transport and related optoelectronic performance, we analysed the empty space in the three crystals (Fig. S21, SI). The crystal lattice of **2,4-OMe** contains 24.4% void space, while those of **3,5-OMe** and **2,6-OMe** have 20.05% and 19.2%, respectively, relative to the respective unit cell volumes. These pores could act as potential trap for the charges and affect conductivity (see below). While the initial charge injection is driven by the applied electric field and quantum mechanical tunnelling, the effective capture and immobilization of the carrier at an attractive trap site (void

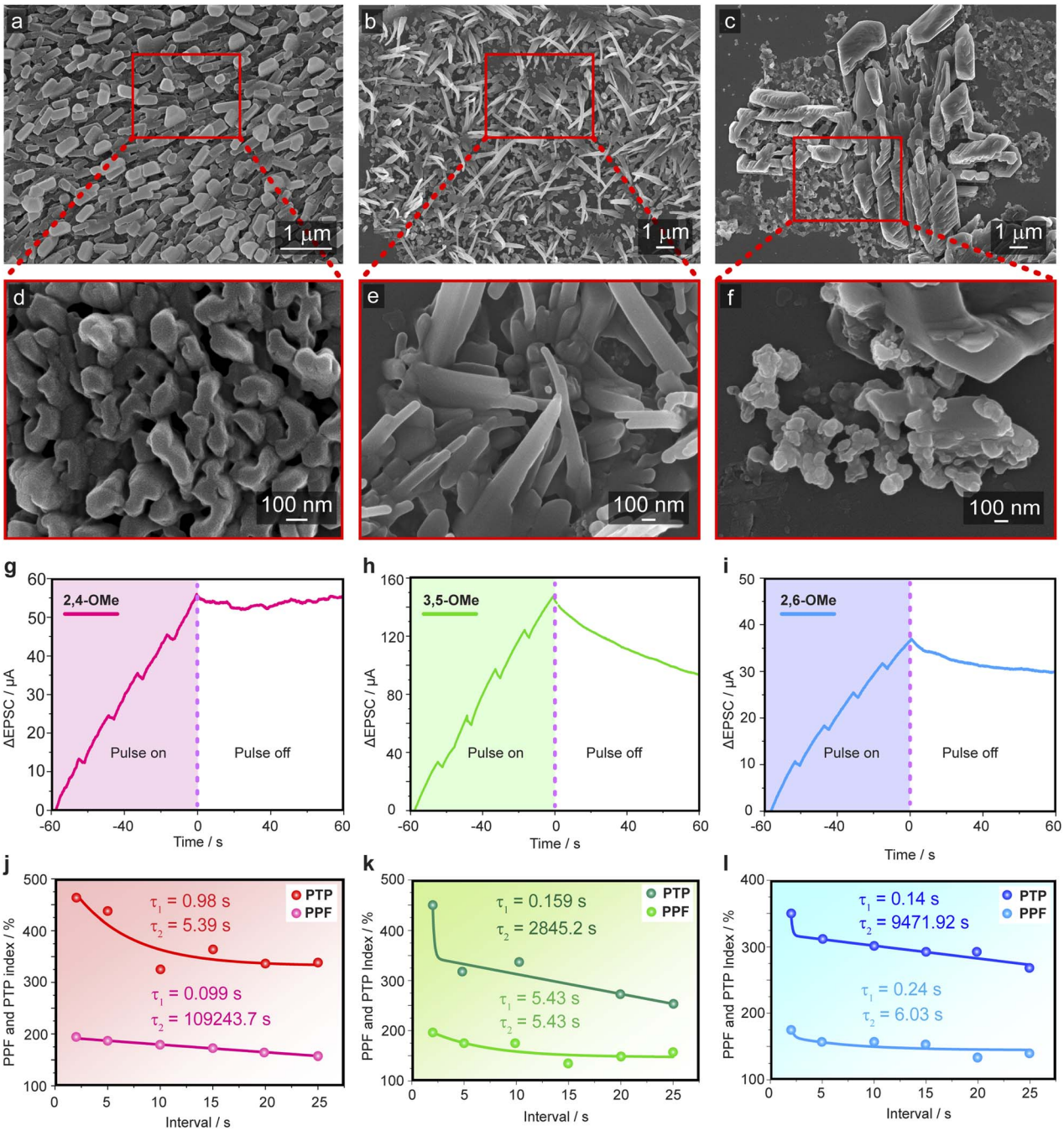

Fig. 4 (a–f) SEM image of drop-cast samples of **3,5-OMe** (a and d), **2,6-OMe** (b and e), and **2,4-OMe** (c and f). (g–i) Changes in EPSC in response to 365 nm pulses, featuring a width of 10 s and 2 s interval at +100 mV bias for **2,4-OMe** (g), **3,5-OMe** (h), and **2,6-OMe** (i) synaptic memory devices. (j–l) Variation of the PPF and PTP indices with pulse intervals for synaptic memory devices based on **2,4-OMe** (j), **3,5-OMe** (k), and **2,6-OMe** (l).

space) are strongly reinforced by intermolecular interactions, coulombic attraction, and dispersive energy. Hirshfeld surface analysis and the related energy framework calculation (Fig. S22–S27, and Tables S3–S9, SI) revealed that **3,5-OMe** and **2,4-OMe** isomers possess higher coulombic interaction energy relative to **2,6-OMe**, which accounts for their better optoelectronic synaptic memory performance (discussed below). Furthermore, non-covalent H···H, C···H, O···H, and N···H interactions present in the structures of **2,4-OMe** and **3,5-OMe** are expected to play pivotal role in lattice stabilization for charge trapping and mobilization that is crucial for optimal device performance and reliability.

The dependence of the fluorescence of these structurally isomeric DAD materials prompted us to explore their potential for optoelectronic synaptic memory applications. To that end, thin film devices were spun-coated on FTO glass (Fig. 1a). The surface morphology of solution-processable thin films (drop-casted on silicon wafer for inspection) was investigated by

scanning electron microscopy (SEM). As shown in Fig. 4a–f, the films display distinct crystalline morphology with variable size and shape of the crystallites for different isomers—an important parameter governing the synaptic memory response in the respective devices. The thickness of the films was measured by SEM analysis (Fig. S28, SI) and the crystallinity of the films was confirmed by X-ray diffraction analysis (Fig. S29, SI). Each device (Fig. 1a) was illuminated with five consecutive UV pulses (365 nm, 8 μW cm^{-2}) under an external bias of +100 mV, during 25 s on/off intervals (Fig. S30, SI). The figures of merit for the photodetection performance of the devices[33] are summarized in Table 1. Each device exhibited excellent photoresponsivity (R) and specific detectivity (D*). Among the three isomers, the device prepared from **3,5-OMe** was found to have optimal performance, with an outstanding photoresponsivity of 41.25 A W^{-1} and a specific detectivity of 4.57×10^{11} Jones.

In the devices based on **2,4-OMe**, the strong intramolecular electronic communication facilitated by favourable donor–acceptor stacking allows a large number of electrons to be photoexcited from the HOMO to the LUMO upon UV illumination. However, the low excited-state lifetime of **2,4-OMe** causes these electrons to rapidly de-excite back to the HOMO before the applied bias can effectively drive them, and therefore result in low photocurrent. The higher photocurrent in the **3,5-OMe**-based devices is attributed to their longer excited-state lifetime, planar molecular structures with enhanced conjugation, and higher coulombic and dispersive energies. The longer lifetime and higher dispersive energy allow photoexcited electrons to be driven by the bias, resulting in stronger current. Conversely, the twisted structure of **2,6-OMe** reduces conjugation and lowers lattice dispersive energy, leading to fewer electrons being excited to the LUMO upon UV illumination. Despite having a longer excited carrier lifetime, the limited number of photoexcited carriers results in the lowest photocurrent among the three device types.

In the photoresponse *I*–*t* curves, all devices demonstrated intriguing behaviour: after the UV light was turned off, the devices did not return to their initial states, but instead the effect of the excitation was sustained (Fig. 4g–i). This observation clearly indicates the potential of the materials for artificial synaptic visual memory applications. Synapses act as bridges for communication of electrical signals between presynaptic and postsynaptic neurons, as schematically depicted in Fig. 1a. External light stimuli, *i.e.*, visual information, are processed by the retina through interconnected neurons and synapses.[21] Given the capabilities of the molecules **2,4-OMe**, **3,5-OMe**, and **2,6-OMe** for "memorizing" visual information, we carried out systematic investigations at an external bias of +100 mV using sequential UV-light pulses (equivalent to presynaptic stimuli) with various intervals and different numbers of pulses. The experiments were carried out by applying five sequential pulses (365 nm, 8 μW cm^{-2}) to the devices with a pulse width (T) of 10 s and an interval (Δt) of 2 s. The results, shown in Fig. 4g–i, evidence significant increase in current under UV illumination, which is attributed to the excitatory postsynaptic current (ΔEPSC). For all devices, the second light pulse (A_2) significantly enhanced the ΔEPSC compared to the initial pulse (A_1). This elevation in postsynaptic response relative to a subsequent presynaptic input established the paired-pulse facilitation (PPF) characteristics of the organic molecules. The PPF behaviour is likely due to the inability of the photogenerated charge carriers to return to their primary state before the arrival of the next pulse; as a result, the newly generated carriers accumulate along with the previously gathered ones, thereby significantly enhancing the ΔEPSC compared to the ΔEPSC induced by the first pulse.[21] After application of five consecutive pulses, the devices were further monitored for another minute (60 s) to test their "memory retention" (Fig. 4g–i). This experiment revealed that **2,4-OMe** could hold the effect of UV-induced external stimuli without a significant loss. Based on these initial investigations, the excellent retention capability of **2,4-OMe** makes it particularly suitable for artificial synapse applications.

Table 1 Performance metrics of the devices under 365 nm wavelength irradiation (8 μW cm^{-2}) at +100 mV bias

Material	Photocurrent/μA	Responsivity/(A W^{-1})	Detectivity/10^{11} Jones
2,4-OMe	13	16.25	2.12
3,5-OMe	33	41.25	4.57
2,6-OMe	10	12.50	2.10

The presynaptic plasticity, which is a measure of the dependence of synaptic response strength on the timing and pattern of the synaptic inputs, can be evaluated through the paired-pulse facilitation (PPF) and post-tetanic potentiation (PTP) indices, which are defined in eqn (1) and (2):

$$\mathrm{PPF} = \frac{A_2}{A_1} \times 100\% \quad (1)$$

$$\mathrm{PTP} = \frac{A_5}{A_1} \times 100\% \quad (2)$$

where A_1, A_2, and A_5 represent the post-synaptic current corresponding to the first, the second, and the fifth pulse, respectively. To study the decay dynamics of the artificial synapses, all the devices were investigated under UV pulses (t = 10 s) with different intervals (Δt = 2, 5, 10, 15, 20, and 25 s). The variations of the PPF and PTP indices are shown in Fig. 4j–l. With the increase in the pulse intervals, both the PPF and PTP indices initially fall drastically, before near saturation for higher time intervals. Both the PPF and PTP indices were fitted using double-exponential decay functions modelled with eqn (3):[21]

$$\mathrm{PPF(or\ PTP)} = C_0 + C_1 \exp\left(-\frac{\Delta t}{\tau_1}\right) + C_2 \exp\left(-\frac{\Delta t}{\tau_2}\right) \quad (3)$$

where the two different time constants t_1 and t_2 are attributed to the characteristic relaxation times corresponding to the rapid and slow decay phases of the synapse, respectively. The extracted values of t_1 and t_2 corresponding to the PPF and PTP indices of all the devices are available from the insets of Fig. 4j–l. For the **2,4-OMe**-based devices, the relaxation times were determined to be 0.099 s/109 243.72 s and 0.98 s/5.39 s, corresponding to the PPF and PTP, respectively. The much lower value of t_1 as compared to t_2 is very similar to the decay

dynamics observed in biological synapses.[34] The **2,6-OMe**-based devices also showed a similar tendency with relaxation times of 0.24 s/6.03 s and 0.14 s/9471.92 s corresponding to the PPF and PTP, respectively. However, for the **3,5-OMe**-based devices, although the decrease of the PTP index with interval time mimicked the biological synapses well (0.159 s/2845.2 s), the PPF index showed a decay that was close to exponential (5.43 s/5.43 s). The very fast "rapid decay phases" ($t_1 = 0.099$ s) and much slower "slow decay phases" ($t_2 = 109\,243.7$ s) favor **2,4-OMe** as the best candidate for artificial synaptic memory applications among the DAD isomers.

The number of incident UV pulses can affect the plasticity of the artificial synaptic memories. To study these effects, namely spike-number-dependent plasticity (SNDP), the devices were illuminated with different numbers (2, 5, 10, and 15) of UV pulses ($T = \Delta t = 10$ s), as shown in Fig. 5a–c, aimed at identifying their synaptic nature and memory retention capability. For the **2,4-OMe**-based devices, the EPSC increases almost linearly with increasing number of pulses (Fig. 5a). However, in the case of the **3,5-OMe** and **2,6-OMe**-based devices, the EPSC tends to saturate with increased number of pulses (Fig. 5b and c). The EPSC corresponding to the first pulse (A_1) and the nth pulse (A_n; $n = 2$, 5, 10, and 15) are depicted in the comparative bar diagrams in Fig. 5d–f. All devices were further observed for another 60 s to verify the effect of the UV-pulses on their plasticity. With increasing number of pulses, the **2,4-OMe**-based devices are able to uphold their long-term plasticity (LTP), whereas in the case of the other two devices the EPSC decreases during post-initiation.

The variation of transient current (current spiked relative to the initial current after n UV pulses) and memory current (the change in current relative to the initial current 60 seconds after switching off the pulses) with the number of pulses is depicted in Fig. 5g–i. Fig. 5g shows that **2,4-OMe**-based devices have very small volatility; they can retain the visual information even after a large number of pulses, which translates into large amount of data. Although **3,5-OMe**- and **2,6-OMe**-based devices also exhibit very good memory retention, their performance is not as

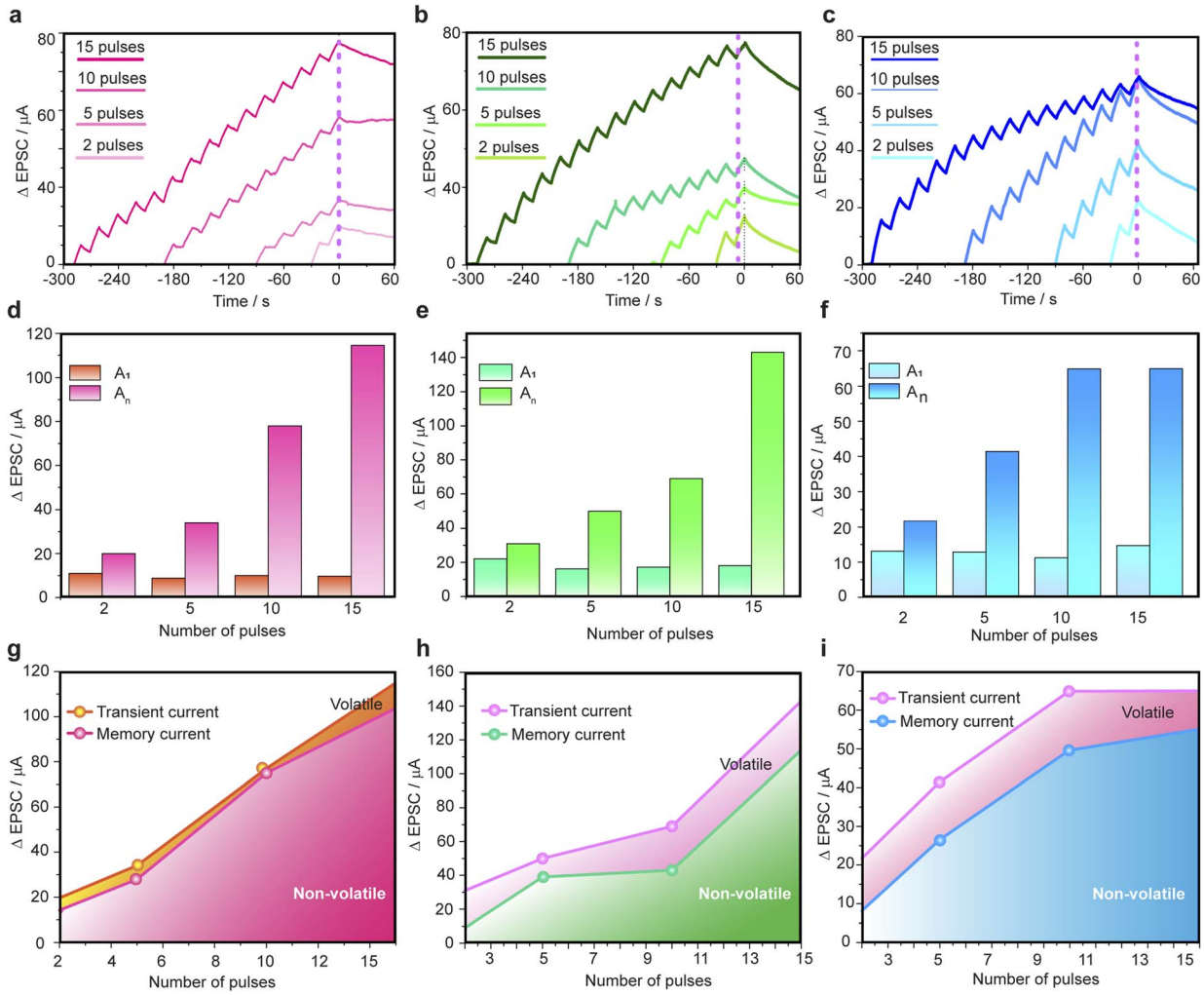

Fig. 5 (a–c) Variations in EPSC in response to different numbers of 365 nm pulses (width of 10 s and interval of 10 s) at +100 mV bias for memory devices based on **2,4-OMe** (a), **3,5-OMe** (b), and **2,6-OMe** (c). (d–f) The EPSC spikes of A_1 and A_n of synaptic memory devices based on **2,4-OMe** (d), **3,5-OMe** (e) and **2,6-OMe** (f). (g–i) Variations of transient current and memory current with different numbers of pulses for synaptic memory devices based on **2,4-OMe** (g), **3,5-OMe** (h), and **2,6-OMe** (i).

efficient relative to **2,4-OMe**. The SNDP gain values (A_n/A_1) show a linear trend with the pulse numbers for **2,4-OMe**-based devices (Fig. S31, SI). The **3,5-OMe**-based devices show a non-linear increasing SNDP gain with the number of pulses, however the SNDP gain of the **2,6-OMe**-based devices is decreasing (Fig. S31, SI).

Persistent photoconductivity (PPC) in crystalline DAD molecules is a complex phenomenon driven by several key factors. The primary mechanisms are trap-assisted charge storage, defect-mediated transport, and structural effects. The intrinsic pores and structural imperfections within the crystalline DAD frameworks, such as vacancies and disordered packing, create high density of localized mid-gap states. These states act as charge traps, capturing photogenerated electrons or holes, as depicted schematically in Fig. 6a and b. The trapping delays the recombination of charge carriers, which are then released slowly after the cessation of light excitation, thereby sustaining conductivity. Additionally, the strong intramolecular charge transfer character brought about by the DAD structure plays a crucial role. Upon light absorption, electrons are promoted from the donor to the acceptor units, creating spatially separated electron–hole pairs that hinder their recombination, thereby prolonging carrier lifetimes and contributing to the persistent conductivity. The retention characteristics of the devices were investigated by illuminating the samples under UV light for 300 s (UV-ON), followed by a 1200 s dark period (UV-OFF). Notably, after 1200 s in the dark, the **2,4-OMe** and **3,5-OMe** devices retain a high fraction of their photocurrent (~62% and ~60%, respectively).[36–38] In contrast, the **2,6-OMe** device exhibits significantly poorer retention (~21%) (Fig. S32, SI), indicating inferior charge storage or trapping stability. The analysis of the void space and energy framework calculation in the structures of the three isomers in Fig. 6c–e reveals distinct differences. The 2,4-isomer exhibits the largest void space at 24.4%, followed by the 3,5-isomer at 20%, and the 2,6-isomer at 19%. Moreover, higher lattice coulombic interaction energy in the 2,4-isomer facilitates stronger charge binding. The superior synaptic memory performance of **2,4-OMe** is a result of a combination of these factors. The highest percentage of voids in its crystalline structure provides large number of charge traps. In conjunction with the high degree of intermolecular charge transfer due to the small slip-angle, this asset favours this material for opto-electronic synaptic memory applications, as described above. In contrast, **2,6-OMe** has the least available void space, smaller coulombic interaction energy and a highly twisted structure, which significantly reduces the conjugation and hinders intramolecular charge transfer, resulting in the weakest PPC performance among the three materials. To gain deeper insight into the trapping/de-trapping dynamics responsible for the persistent photocurrent (PPC) behavior, the time-dependent current response in both the growth (UV-ON) and decay (UV-OFF) regimes was analysed using a bi-exponential fitting function (eqn (4)). Such a response is widely regarded as a hallmark of heterogeneous trap distributions and multi-scale charge relaxation processes.[35]

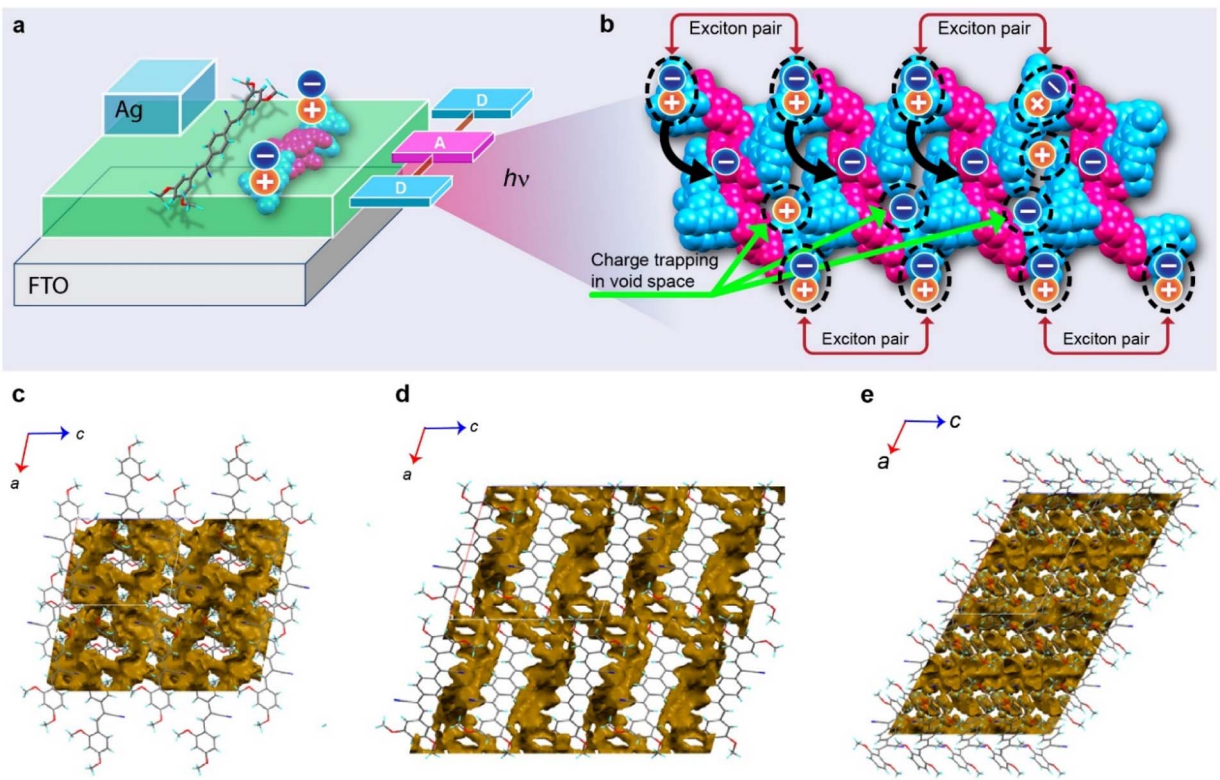

Fig. 6 (a and b) Possible mechanistic model of the photosynaptic behaviour in DAD isomers. (c–e) Pore analysis of **2,4-OMe** (c), **3,5-OMe** (d), and **2,6-OMe** (e).

$$I = I_0 + A_f e^{-\frac{t}{\tau_f}} + A_s e^{-\frac{t}{\tau_s}} \quad (4)$$

Here, τ_f and τ_s represent the fast and slow response time constants, respectively, while A_f and A_s are the corresponding pre-exponential coefficients. The underlying mechanism of the persistent photocurrent (PPC) behavior is schematically illustrated in Fig. S33, SI. During the rising phase (UV-ON), the fast component is attributed to the prompt photoexcitation of charge carriers from the HOMO to the LUMO, whereas the slow component originates from the gradual filling of trap states. In contrast, during the decay phase (UV-OFF), the fast time constant corresponds to the rapid recombination of free carriers, while the slow component is associated with the delayed release (detrapping) of carriers from trap states. Notably, deep trap states, located further within the bandgap, require higher thermal activation energy for carrier release, resulting in a significantly prolonged decay process and slower recovery of the dark current.[39–43] The extracted fitting parameters for all three samples are summarized in the Table S10, SI. The fitting parameters presented in the table indicate that, during the rising phase, the photoresponse of the **2,4-OMe** and **3,5-OMe** devices is predominantly governed by the trap-filling process, suggesting a substantial population of charge carriers being captured by both shallow and deep trap states. In contrast, the **2,6-OMe** device exhibits a response primarily dominated by direct photogeneration, corresponding to charge carrier transitions from the HOMO to the LUMO. Owing to its relatively inferior molecular conjugation, **2,6-OMe** displays a comparatively larger time constant associated with the photogeneration process. Furthermore, the minimal contribution of the trap-filling component during the rising phase indicates a significantly reduced density of accessible trap states, leading to negligible charge trapping during photoexcitation in the **2,6-OMe** device. During the falling phase, the decay dynamics for all devices are predominantly governed by thermally activated detrapping of charge carriers from both deep and near band-edge trap states. Although the fitting parameters for the **2,6-OMe** device also indicate a nominal dominance of the detrapping process during de-excitation, its overall retention remains the lowest (~21%). This apparent discrepancy arises from the minimal charge trapping during the photoexcitation stage, resulting in a significantly reduced population of stored carriers available for delayed release. Consequently, despite the presence of detrapping dynamics, the limited trap occupancy in **2,6-OMe** leads to a much weaker persistent photocurrent response.

To probe the thermally activated, near-band-edge trap-assisted charge transport mechanism, temperature-dependent current–voltage (I–V) measurements were carried out, as presented in Fig. S34 and S35, SI. The thermal activation energy (E_a) was subsequently extracted from the temperature-dependent I–V characteristics using the Arrhenius relation (eqn (5)):

$$\ln(\sigma) = \ln(\sigma_0) - \frac{E_a}{KT} \quad (5)$$

Here, σ represents the electrical conductance, extracted from the slope of the linear region of the I–V characteristics, while k_B and T denote the Boltzmann constant and absolute temperature, respectively. The thermal activation energy (E_a) was determined from the slope of the $\ln(\sigma)$ *versus* $1/k_BT$ plot. The extracted activation energies for the **2,4-OMe**, **3,5-OMe**, and **2,6-OMe** devices are 86.41 meV, 98.89 meV, and 50.27 meV, respectively. The relatively higher E_a values for the **2,4-OMe** and **3,5-OMe** devices indicate the presence of deeper near-band-edge trap states, whereas the lower activation energy in **2,6-OMe** suggests comparatively shallower traps or reduced trap-assisted transport.

Conclusions

In this work, we report a series of synthetically simple isomeric donor–acceptor–donor (DAD) triads that display an excellent synaptic memory response with a two-electrode system under light illumination. The synaptic response can be tuned by simply changing the position of the donor -OMe groups in the DAD molecule and thereby integrating molecular engineering with device performance. The best performing DAD isomer, **2,4-OMe**, successfully emulates a biological synaptic behaviour with a PPF index of approximately 196% when subjected to a 10-second UV light pulse illuminated at an interval of 2 seconds. Other synaptic characteristics, such as EPSC, IPSC, and ENDP, were also demonstrated in this memory device, and within a more general context they establish a novel approach toward organic optoelectronic neuromorphic computing.

Experimental and theoretical procedures

Materials

2,6-Dimethoxybenzaldehyde and *p*-xylylene dicyanide were purchased from TCI India. 2,4-Dimethoxybenzaldehyde and 3,5-dimethoxybenzaldehyde were purchased from Sigma Aldrich and were used as received. Merck ACS-grade solvents were used for the syntheses, and spectroscopy grade solvents were used for crystallization and all spectroscopic studies.

^{1}H NMR and ^{13}C NMR

The ^{1}H NMR and ^{13}C NMR spectra were recorded on a Bruker AVANCE 300 spectrometer (400 MHz) using $CDCl_3$ as the solvent. The shifts (δ) are given in ppm.

HRMS

The high-resolution mass spectra (HRMS) of the compounds were recorded on a QTOF Micro YA263 mass spectrometer in electrospray ionization (ESI) mode.

UV-Vis and fluorescence spectroscopy

The solution and solid-state UV-Vis absorption spectra were recorded with a Shimadzu UV-2401C spectrophotometer. The solid-state absorption spectra were recorded with sample coated (thin film) quartz plates. All emission spectra were recorded on a HORIBA Jobin Yvon Fluorolomax-4

spectrofluorometer in the solid state using a solid-state sample holder, and the data were collected in front face mode.

Fluorescence lifetime

Time-resolved emission measurements of solid crystalline powder samples were carried out on a modular time-correlated single photon counting (Horiba) spectrometer equipped with a Delta Flex detector PPD850.

Scanning electron microscopy (SEM)

SEM images of the sample were recorded on a ZEOL-JSM-7610F Schottky field emission scanning electron microscope. Samples (2 mg per 1 mL DMF solution) were drop-casted on a silicon wafer and dried under ambient conditions to prepare a film. The film samples were gold-coated prior to the SEM experiment. For the film thickness study, the film-coated glass slide was attached to a vertical sample holder, and the images were collected in a vertical sample geometry.

FT-IR

The IR spectra of the DAD crystals were recorded in a Parkin Elmer LX-1 FT-IR spectrometer in ATR mode.

Powder X-ray diffraction (PXRD)

PXRD data of the compounds **3,5-OMe**, **2,4-OMe** and **2,6-OMe** were collected on a Bruker D8 Advance diffractometer with Cu K_α radiation ($\lambda = 1.5418$ Å), operating at 40 kV and 40 mA. The Lynxeye detector was utilized for data acquisition with a scanning rate of 0.2 seconds per step over a 2θ range of 0° to 50°. For checking the crystallinity of the thin films, the sample solution (2 mg mL^{-1}) was drop-casted on a glass plate kept at 50 °C (on a hotplate) and dried there in open air for 30 minutes. The dried samples were then subjected to analysis.

Single-crystal X-ray diffraction analysis

The single-crystal XRD data of all compounds were collected using a Microfocus D8 venture APEX 3 diffractometer (Bruker) equipped with a CCD area detector and by using MoK_α radiation ($\lambda = 0.71069$ Å). The SAINT (v. 8.38A) program was used for data reduction, which was then analysed using XPREP (APEX 3, ver. 2017.3-0).[44] The SADABS program was used for absorption correction.[45] The structures were solved by SHELXT (version 2018/2)[46] and refined by using SHELXL-2014 included in the APEX 3 suite.[47–50] All non-hydrogen atoms were refined anisotropically, whereas the positions of the hydrogen atoms were calculated and refined isotopically. The crystallographic data for **3,5-OMe**, **2,4-OMe** and **2,6-OMe** have been deposited with the Cambridge Crystallographic Data Centre (CCDC) under deposition no. 2304045, 2304044 and 2359645, respectively. Pore analysis of the crystals and the preparation of crystallographic graphics/images were carried out using Mercury.[51]

Theoretical calculations

All of the theoretical calculations were carried out using the Gaussian 16 program suite.[52] Density functional theory (DFT) with hybrid B3LYP functionals[53–55] and the 6-31G(d,p) basis set was used for gas-phase geometry optimization of the compounds by using input coordinates from respective crystal structures. TDDFT calculations were carried with the hybrid CAM-B3LYP functional and 6-31G(d,p) basis set.[56] Tomasi's polarizable continuum model (PCM) was used for describing the solvent effect on the HOMO–LUMO gap of the compound. The output structures were visualized by using the Chemcraft software.[57]

Synthetic procedure

Synthesis of 2,4-OMe

A 100 mL round-bottom flask was charged with 2,4-dimethoxybenzaldehyde (0.332 g, 2 mmol) and *p*-xylene dicyanide (0.157 g, 1 mmol) in 30 mL of methanol, along with potassium *t*-butoxide (0.5 g). Additionally, 5–6 drops of tetrabutylammonium hydroxide (TBAH) were added to the reaction mixture. The resulting mixture was heated at 70 °C for 4 h. The product mixture was filtered and the crude was dried in air to obtain a yellow-coloured solid product of **2,4-OMe** (0.293 g, 65%). Slow evaporation of the crude product from $CHCl_3$ solution yielded prismatic yellow-coloured crystals, which were segregated under an optical microscope and dried in air. ^{1}H NMR (400 MHz, $CDCl_3$, δ in ppm): 8.26 (d, $J = 9.0$ Hz, 1H, Ar$\underline{H}$), 7.98 (s, 1H, $\underline{H}$C-N), 7.74 (s, 1H, Ar$\underline{H}$), 6.63 (q, 4H, Ar$\underline{H}$), 6.51 (d, 1H, Ar$\underline{H}$), 3.90 (s, 6H, OC$\underline{H}_3$). HRMS calculated for $C_{28}H_{24}N_2O_4$ is 453.1736, obtained $m/z = 453.1816$. (M + 1). Melting point: 216−221 °C.

Synthesis of 2,6-OMe

A 100 mL round-bottom flask was charged with 2,4-dimethoxybenzaldehyde (0.333 g, 2 mmol) and *p*-xylylene dicyanide (0.157 g, 1 mmol) in 30 mL of methanol, along with potassium *t*-butoxide (0.5 g). Additionally, 5–6 drops of tetrabutylammonium hydroxide (TBAH) were added to the reaction mixture. A catalytic amount of glacial acetic acid was added to this solution, and the resulting mixture was heated at 90 °C for 4 h. The product mixture was filtered and the crude was dried in air. Prismatic pale-yellow crystals of **2,6-OMe** were obtained from DMSO after 20 days, which were segregated and dried in air (0.316 g, 70%). ^{1}H NMR (400 MHz, $CDCl_3$, δ in ppm): 8.26 (d, $J = 9.0$ Hz, 1H, Ar$\underline{H}$), 7.98 (s, 1H, $\underline{H}$C-N), 7.28 (t, 1H, Ar$\underline{H}$), 6.58 (q, 4H, Ar$\underline{H}$), 3.85 (s, 6H, OC$\underline{H}_3$). HRMS calculated for $C_{28}H_{24}N_2O_4$ is 453.1736, obtained $m/z = 453.1814$ (M + 1). Melting point: 190−196 °C.

Synthesis of 3,5-OMe

A 100 mL round-bottom flask was charged with 3,5-dimethoxybenzaldehyde (0.332 g, 2 mmol) and *p*-xylylene dicyanide (0.157 g, 1 mmol) in 30 mL of methanol, along with potassium *t*-butoxide (0.5 g). Additionally, 5–6 drops of tetrabutylammonium hydroxide (TBAH) were added to the reaction mixture. A catalytic amount of glacial acetic acid was added to this solution, and the resulting mixture was heated at 90 °C for 4 h. The product mixture was filtered and the crude was dried in

air. Prismatic bright green crystals of **3,5-OMe** were obtained from DMSO after 15 days, which were segregated and dried in air (0.343 g, 76%). ^{1}H NMR (400 MHz, $CDCl_3$, δ in ppm): 7.78 (d, J = 8 Hz, 2H, Ar*H*), 7.60 (s, 1H, *H*C-N), 7.11 (t, 1H, Ar*H*), 6.59 (q, 4H, Ar*H*), 3.88 (s, 6H, OC*H*$_3$). HRMS calculated for $C_{28}H_{24}N_2O_4$ is 453.1736, obtained m/z = 453.1814 (M + 1). Melting point: 190–196 °C.

Crystallization of DAD isomers

Prismatic yellow-coloured crystals of **2,4-OMe** crystals were obtained by slow evaporation of $CHCl_3$ solution at room temperature. Prismatic pale-yellow coloured crystals of **2,6-OMe** crystals were obtained from DMSO solution by keeping the solution at room temperature for 20 days. **3,5-OMe** crystals were obtained from DMSO solution kept room temperature for 15 days, which led to the growth of prismatic bright green-coloured crystals.

Device preparation

The synaptic memory devices were fabricated *via* a simple spin-casting method. The DAD isomer crystals were each dissolved in DMF (2 mg mL^{-1}) to prepare the inks for spin-coating. The inks were spin-coated at a speed of 1500 rpm for 15 s on pre-cleaned FTO coated glass, keeping a small portion bare by using non-adhesive Teflon tape, followed by drying on a hotplate at 60 °C for 2 minutes. The spin coating and drying processes were repeated 10 times. Finally, the devices were completed by painting top and bottom electrodes on the film and the bare portion on the FTO by using highly conducting Ag paste (Techinstro). The final devices are shown schematically in Fig. 1a.

Author contributions

M. P. and P. N. designed the DAD molecules and its positional isomers. M. B. and D. D. have performed synthesis and characterizations of the compounds. R. N. G. designed the optoelectronic experiments and M. K. carried out the optoelectronic studies. M. B., D. D. and M. K. contributed equally to this work. M. P., P. N. and R. N. G. conceived the study and co-wrote the paper. All the authors have read and approved the final version of the manuscript.

Conflicts of interest

There are no conflicts to declare.

Data availability

CCDC 2304044 (**2,4-OMe**), 2304045 (**3,5-OMe**) and 2359645 (**2,6-OMe**) contain the supplementary crystallographic data for this paper.[58a–c]

Supplementary information (SI): synthetic scheme and all the characterization data (^{1}H NMR, ^{13}C NMR, HRMS, IR), UV-Vis and fluorescence spectroscopic plots, PXRD data, tables for single crystal X-ray crystallographic parameters, details of Hirshfeld surface analysis data and related plots, and other additional figures. Single crystal X-ray data have been deposited under CCDC numbers 2304044, 2304045 and 2359645 which are available under website https://www.ccdc.cam.ac.uk/structures/, or *via* email to data_request@ccdc.cam.ac.uk, or by contacting Cambridge Crystallographic Data Centre, 12 Union Road, Cambridge CB2 1EZ, UK; fax +44 1223 336033. See DOI: https://doi.org/10.1039/d6sc01505k.

Acknowledgements

M. K. P. acknowledges SERB India, for a start-up research grant (F. No. SRG/2020/000943) and UGC, New Delhi, India, for a start-up research grant (No. F.30-530/2020(BSR)). MB thanks the SVMCM scholarship, Govt of West Bengal, for a fellowship. DD thank the Council for Scientific and Industrial Research (CSIR), New Delhi, for a fellowship. M. K would like to thank UGC, Govt. of India, for providing a research fellowship (NTA ref. no. 211610081286). R. N. G wishes to thank the Science and Engineering Research Board, Govt. of India (File no. – EEQ/2023/000219), for financial support. This project was partially funded by New York University Abu Dhabi (AD073). Additionally, this material is based on work supported by Tamkeen under NYUAD RRC Grant No. CG011.

References

1 J. Wang, Y. Lin, J. You, T. Yu, W. Meng and L. Sun, *Adv. Intell. Syst.*, 2025, 2401057.
2 Y. Zhang, Z. Ma, Z. Chen, S. Poddar, Y. Zhu, B. Han, C. L. J. Chan, Y. Ding, X. Kong and Z. Fan, *Adv. Intell. Syst.*, 2024, **6**, 2300586.
3 R. Shenoy, A. Tudor, D. Nathan, A. Deo, Z. Rong, C. M. Shaffer, C. D. Danesh, B. Suresh and Y. Chen, *Adv. Intell. Syst.*, 2022, **4**, 2200105.
4 L. Zhang, H. Yu, C. Xiao, J. Si, H. Xu, W. Zhu and L. Wang, *Adv. Electron. Mater.*, 2021, **7**, 2000945.
5 M. K. Hota, M. N. Hedhili, N. Wehbe, M. A. McLachlan and H. N. Alshareef, *Adv. Mater. Interfaces*, 2016, **3**, 1600192.
6 E. E. Josberger, Y. Deng, W. Sun, R. Kautza and M. Rolandi, *Adv. Mater.*, 2014, **26**, 4986–4990.
7 D. Sarkar, J. Tao, W. Wang, Q. Lin, M. Yeung, C. Ren and R. Kapadia, *ACS Nano*, 2018, **12**, 1656–1663.
8 J. Yang, H. Cho, R. Ryu, M. Ismail, C. Mahata and S. Kim, *ACS Appl. Mater. Interfaces*, 2021, **13**, 33244–33252.
9 T. Zhang, C. Fan, L. Hu, F. Zhuge, X. Pan and Z. Ye, *ACS Nano*, 2024, **18**, 16236–16247.
10 S. L. Gao, L. P. Qiu, J. Zhang, W. P. Han, S. Ramakrishna and Y. Z. Long, *ACS Appl. Electron. Mater.*, 2024, **6**, 1542–1561.
11 V. M. Poole, S. J. Jokela and M. D. McCluskey, *Sci. Rep.*, 2017, **7**, 6659.
12 Z. Xiao and J. Huang, *Adv. Electron. Mater.*, 2016, **2**, 1600100.
13 M. Loizos, K. Chatzimanolis, K. Anagnostou, K. Rogdakis and E. Kymakis, *ACS Appl. Electron. Mater.*, 2025, **8**, 3610.
14 B. Pillai, P. De Souza and M. Merlyne, *ACS Appl. Mater. Interfaces*, 2017, **9**, 1609–1617.

15 M. Farronato, P. Mannocci, M. Melegari, S. Ricci, C. M. Compagnoni and D. Ielmini, *Adv. Mater.*, 2023, **35**, 2205381.
16 Y.-C. Chiang, C.-C. Hung, Y.-C. Lin, Y.-C. Chiu, T. Isono, T. Satoh and W.-C. Chen, *Adv. Mater.*, 2020, **32**, 2002638.
17 T.-W. Chang, Y.-S. Li, N. Matsuhisa and C.-C. Shih, *J. Mater. Chem. C*, 2022, **10**, 13372.
18 C. Zheng, C. Li, H. S.-T. Yuan and Y. Zhou, *Adv. Electron. Mater.*, 2020, **6**, 2000641.
19 H. Roh, H. Yue, H. Shuwen, C. K. Hang, H. Kulik and A. Gumyusenge, *Adv. Funct. Mater.*, 2023, **33**, 2304893.
20 L. Wang, C. Zheng, J. Fu, J. Hua, J. Chen, J. Gao, H. Ling, L. Xie and W. Huang, *Adv. Electron. Mater.*, 2022, **8**, 2200155.
21 H. Guo, J. Guo, Y. Wang, H. Wang, S. Cheng, Z. Wang, Q. Miao and X. Xu, *ACS Appl. Mater. Interfaces*, 2024, **16**, 66948–66960.
22 J. Zhang, D. Liu, S. Shi, Q. Yang, B. Yang, P. Guo, L. Fang, S. Dai, L. Xiong and J. Huang, *npj Flexible Electron.*, 2022, **6**, 30.
23 M. M. H. Tanim, Z. Templin and F. Zhao, *Micromachines*, 2023, **14**, 235.
24 Z. Feng, M. Comi, Y. Ren, D. Sredojevic, S. Attar, J. Yang, Z. Wang, R. Chen, S. Han, M. Al-Hashimi and Y. Zhou, *J. Mater. Chem. C*, 2022, **10**, 16604.
25 K. Chen, H. Hu, H. B. Gobeze, W. J. Lee, A. Abtahi, K. S. Schanze and J. Mei, *Nat. Photonics*, 2023, **17**, 629–637.
26 Y. Lee and T. W. Lee, *Acc. Chem. Res.*, 2019, **52**, 964–974.
27 S. Liu, J. Zeng, Z. Wu, H. Hu, A. Xu, H. Huang, W. Chen, Z. Yu, Y. Zhao, R. Wang, T. Han, C. Li, P. Gao, H. Kim, S. J. Baik, R. Zhang, Z. Zhang, P. Zhou and G. Liu, *Nat. Commun.*, 2023, **14**, 7655.
28 T. F. Yu, H. Y. Chen, M. Y. Liao, H. C. Tien, T. T. Chang, C. C. Chueh and W. Y. Lee, *ACS Appl. Mater. Interfaces*, 2020, **12**, 33968–33978.
29 R. Jia, X. Wu, W. Deng, X. Zhang, L. Huang, K. Niu, L. Chi and J. Jie, *Adv. Funct. Mater.*, 2019, **29**, 1905657.
30 Y. Chen, H. Wang, Y. Yao, Y. Wang, C. Ma and P. Samorì, *Adv. Mater.*, 2021, **33**, 2103369.
31 H. Chen, Y. Cai, Y. Han and H. Huang, *Angew. Chem., Int. Ed.*, 2024, **63**, e202313634.
32 C. Eckel, J. Lenz, A. Melianas, A. Salleo and R. T. Weitz, *Nano Lett.*, 2022, **22**, 973–979.
33 M. Kangsabanik, R. Sarkar, J. Chowdhury and R. N. Gayen, *J. Alloys Compd.*, 2025, **1010**, 177758.
34 S. Feng, J. Li, L. Feng, Z. Liu, J. Wang, C. Cui, O. Zhou, L. Deng, H. Xu, B. Leng, X. Q. Chen, X. Jiang, B. Liu and X. Zhang, *Adv. Mater.*, 2023, **35**, 2308090.
35 P. Rajabi Kalvani, A. Parisini, M. Pavesi, *et al.*, *Adv. Electron. Mater.*, 2025, **11**, e00072.
36 J. Kim, E. C. Park, W. Shin, R.-H. Koo, C.-H. Han, H. Y. Kang, T. G. Yang, Y. Goh, K. Lee, D. Ha, S. S. Cheema, J. K. Jeong and D. Kwon, *Nat. Commun.*, 2024, **15**, 9147.
37 D. Cai, J. Wang, T. Zhao, M. Shen, Y. Liu, T. Zhang, F. Zhang, Y. Wang, Y. Jiang and D. Gu, *Adv. Sci.*, 2026, **13**, e11168.
38 Y. Li, J. Lu, D. Shang, Q. Liu, S. Wu, Z. Wu, X. Zhang, J. Yang, Z. Wang, H. Lv and M. Liu, *Adv. Mater.*, 2020, **32**, 2003018.
39 H. Zhou, L. Cong, J. Ma, B. Li, M. Chen, H. Xu and Y. Liu, *J. Mater. Chem. C*, 2019, **7**, 13149.
40 K. Liu, M. Sakurai, M. Aono and D. Shen, *Adv. Funct. Mater.*, 2015, **25**, 3157.
41 V. M. Kalygina, A. V. Tsymbalov, A. Almaev, B. O. Kushnarev, V. L. Oleinik, J. V. Petrova and P. A. Yunin, *IEEE Sens. J.*, 2023, **23**, 15530.
42 S. Nandi, S. Ghosal, M. Meyyappan and P. K. Giri, *Mater. Horiz.*, 2025, **12**, 4274–4288.
43 Z. Ren, S. Wang, B. Meng, H. Liu, Q. An, L. Su and R. Chen, *ACS Appl. Mater. Interfaces*, 2026, **18**, 6191–6199.
44 Bruker AXS Inc., *APEX3, Version 2017.3-0; SAINT, Version 8.38A*, Bruker AXS Inc., Madison, WI, 2012, https://www.bruker.com.
45 G. M. Sheldrick, *SADABS, University of Göttingen, Göttingen, Germany, 1996; part of Bruker APEX3 software package (Version 2017.3-0)*, Bruker AXS, Madison, WI, 2017.
46 G. M. Sheldrick, *SHELXTL XT – Crystal Structure Solution, Version 2014/4*, Bruker AXS, Madison, WI, 2014.
47 G. M. Sheldrick, *SHELXL-2014*, University of Göttingen, Göttingen, Germany, 2014.
48 G. M. Sheldrick, *Acta Crystallogr., Sect. A*, 2015, **71**, 3–8.
49 G. M. Sheldrick, *Acta Crystallogr., Sect. A*, 2008, **64**, 112–122.
50 H. Liu, *Acta Crystallogr., Sect. E: Struct. Rep. Online*, 2010, **66**, o1582.
51 C. F. Macrae, I. Sovago, S. J. Cottrell, P. T. A. Galek, P. McCabe, E. Pidcock, M. Platings, G. P. Shields, J. S. Stevens, M. Towler and P. A. Wood, *J. Appl. Crystallogr.*, 2020, **53**, 226–235.
52 M. J. Frisch *et al.*, *Gaussian 16, Revision A.03*, Gaussian, Inc., Wallingford, CT, 2016.
53 A. D. Becke, *Phys. Rev. A*, 1988, **38**, 3098–3100.
54 C. Lee, W. Yang and R. G. Parr, *Phys. Rev. B: Condens. Matter Mater. Phys.*, 1988, **37**, 785–789.
55 M. Cossi, V. Barone, R. Cammi and J. Tomasi, *Chem. Phys. Lett.*, 1996, **255**, 327–335.
56 T. Yanai, D. P. Tew and N. C. Handy, *J. Chem. Phys.*, 2004, **124**, 104106.
57 Chemcraft, Version 1.8 (Build 682), https://www.chemcraftprog.com.
58 (*a*) CCDC 2304044: Experimental Crystal Structure Determination, 2026, DOI: 10.5517/ccdc.csd.cc2hbk0f; (*b*) CCDC 2304045: Experimental Crystal Structure Determination, 2026, DOI: 10.5517/ccdc.csd.cc2hbk1g; (*c*) CCDC 2359645: Experimental Crystal Structure Determination, 2026, DOI: 10.5517/ccdc.csd.cc2k6dls.